How defects depend on geometry and scanning strategy in additively manufactured AlSi10Mg

Lukas Englert *, Steffen Czink, Stefan Dietrich, Volker Schulze

Institute for Applied Materials (IAM-WK), Engelbert-Arnold-Straße 4, 76131 Karlsruhe, Germany

Keywords:
Porosity
Scan strategy
Downskin
Selective laser melting
Melt pool instability
Lack of fusion
Powder bed fusion

A B S T R A C T

Porosity is an inherent feature of additively manufactured components that impairs the mechanical properties. Since porosity depends not only on the process parameters but also on the component geometry, it is necessary to investigate this dependency. This study reveals relationships between porosity, process parameters and component geometry in AlSi10Mg specimens. Micro-computed tomography images of different geometries built with varying parameters were analysed for pore concentrations. The quantity and distribution of pores at overhangs depends on the laser scan speed and the width of the overhang. Similarly, the scan speed influences the effective bead width and thus the pore formation at thin structures. This relationship is revealed by an in-depth analysis of the laser path together with the μCT images. The investigations show that the process parameters can only be optimal for a specific geometry. The presented interdependencies can be used to derive locally adjusted scanning strategies and machine parameters.

1. Introduction

Laser powder bed fusion (LPBF) has gained immense importance as an additive manufacturing (AM) process for structural metallic components. The high geometric complexity of such components has promoted LPBF as rapidly evolving technique in many industrial fields. This rapid development has led to a large number of microstructure related questions and problems especially regarding a controllable and reproducible low porosity in the process. Due to the inevitable occurrence of such defects from processing, the correlation of the material analysis and quality assurance in AM with the manufacturing parameters and component geometries is still a key aspect under research. The starting point for improving the properties of additively manufactured materials is usually a density optimisation through a parametric process study. In LPBF, optimising process parameters is mostly comprised of tuning laser power, scan speed and scan line spacing by fabricating small test cubes until a high specific density of the cubes is reached (see for example the study conducted by Aboulkhair et al. (2014)). Different mechanisms can lead to a variety of defects. For example, Aboulkhair et al. (2014) examined cross sections of additively manufactured cubes of AlSi10Mg. Too high line spacing led to large pores between the scan tracks, whereas density of the cubes increased with smaller line spacing.

Matthews et al. (2016) used high speed video to gain insight how vaporising of material through the laser creates shear gas flow that ultimately leads to denudation of powder near the melt track as the gas flow entrains the powder. This lack of powder eventually leads to defects in the built parts. Martin et al. (2019) used high-speed X-ray imaging to show how deactivation or deceleration of the laser spot at the end of a trajectory leads to the creation of a keyhole pore. When the laser is deactivated or the spot is moved away from this point, molten material flows into the capillary and prevents entrapped shielding gas from escaping which forms a keyhole pore. Another mechanism of defect formation is the balling phenomenon. Depending on the used scan speed, the shape of the molten pool varies and at high scan speed the molten zone elongates and finally separates into spherical balls through the Plateau-Rayleigh instability. A review on this topic is given by DebRoy et al. (2018). The interplay between the different effects involved (for example incomplete melting, Marangoni convection, particle spatter through material vaporisation and powder denudation) is key to dense parts and can be adjusted by changing the process parameters mentioned. Simplifications of process parameters such as line or volumetric energy densities are often used to assess printing parameters. Scipioni Bertoli et al. (2017) tested the applicability of this simplification by producing and comparing individual melt tracks with the same energy density but different process parameters. It was found that the shape of this tracks varied and energy density could not be used

* Corresponding author.
E-mail address: lukas.englert@kit.edu (L. Englert).

to describe occurring defects. Prashanth et al. (2017) similarly fabricated specimens from AlSi12 with constant energy density but different process parameters and measured specimen density. With decreasing laser power, the density of the specimens reduced regardless of energy density. Therefore, a detailed analysis of the influence of the process parameters on the occurring defects is considered important.

A convenient way of examining which pore formation mechanisms are to blame for occurring porosity is micro-computed tomography (μCT). Du Plessis (2019) investigated the development of different pore formation mechanisms over a range of process parameters in LPBF Ti6Al4V using micro-computed tomography. Lack of fusion pores occurred upon increasing the hatch spacing. Since the scan pattern was rotated in subsequent layers, the voids between the tracks formed a polygonal pattern exhibiting the rotation angle. Depending on the scan speed used, the amount of keyhole pores increased. A high scan speed allowed a wider range of power settings to achieve low porosity values, as also reported from Cunningham et al. (2019) through the use of high-speed X-ray imaging. This was explained by a reduction of keyhole instability at high scan speeds. Hastie et al. (2020) fabricated specimens from AlSi10Mg and characterised the shape and quantity of pores through μCT. Depending on the process region investigated, different pore morphologies were found. The defects were classified into shape categories based on their relative dimensions. The analysis showed how this shape analysis can be used irrespective of the global porosity to observe the transition between irregular lack of fusion pores and spherical gas pores when the applied energy density is increased.

In additively manufactured parts, the quality of the solidified material is inherently coupled to the geometry of the built part. Sanaei et al. (2019) studied defect distributions in LPBF samples and found defect critical pore concentrations near the surface of specimens while optimisation of process parameters reduced defect variability. Léonard et al. (2012) assessed defect distribution in SEBM titanium parts. It was found that the distribution of small spherical gas pores was not affected by the specimen geometry or its orientation. On the contrary larger defects were not spread evenly through the parts but on certain near surface positions depending on component geometry and building orientation. Piazza et al. (2020) investigated differences between LPBF parts with a conical and a cylindrical shape made of 316L steel. Higher densities were measured in the conical geometry, which was explained by the geometrically induced misalignment of the laser paths in successive layers.

A number of studies have focused also on the influence of built geometry size on mechanical properties of the built specimens. For example, Takata et al. (2018) investigated sample size dependence of the microstructure and found a slight softening effect with decreasing sample size. Roach et al. (2020) found a correlation of mechanical properties with specimen size of LPBF 316L, because build quality influenced by specimen size played a major role in reducing the effective load bearing area in smaller specimens. Dong et al. (2018) found variation in mechanical properties of different diameter AlSi10Mg specimens. The findings of the study were that small specimens exhibited finer microstructure and lower yield strength.

The small amount of literature with respect to the interplay of pore architecture, process parameters and part geometry indicates, that it is largely unclear how part geometry influences defect distribution and how such issues can be mitigated by process control. Therefore, the aim of this work is to provide detailed insight into the effects of process parameters on the microstructure of component-like test specimens by using μCT methods and to investigate geometry induced changes in prevalent defects.

2. Materials and methods

2.1. Additive manufacturing and specimen geometries

AlSi10Mg supplied from m4p material solutions GmbH with a D50 of 35.3 μm and a D90 of 57.5 μm was used for manufacturing the samples shown in this publication. The powder was gas atomised. The chemical composition is shown in Table 1. The powder bulk density is specified as 1.50 g cm^{-3}. Fig. 1 shows a cross section of the powder. The powder particles are mostly spherical or elliptical in shape.

The.stl files of the samples were sliced using ORLAS Suite version 6.1.0.13 (O.R. Lasertechnologie GmbH, 2021) and manufactured on an ORLAS Creator from O.R. Laser Technologie GmbH, which features a 250 W Yb fibre laser. Given the objective of the present work, different process parameters were used to manufacture specimens and are provided at the respective section where the results are presented. Nonetheless, all samples were manufactured without platform heating, using Argon as shielding gas, 30 μm layer height and a nominal laser spot diameter of 40 μm, which are common parameters. The samples were sliced with two perimeters and the linear hatching strategy with 67° layer rotation without using "skywriting". The terms used for describing the scan parameters are explained in Fig. 2. Visualisation and analysis of laser path features was carried out using the in-house developed software GCode2vtk, which is used to extract information from the G-code and generate a.vtk file, that can be opened in Paraview (Ahrens et al., 2005). The.vtk file contains the toolpath trajectory and metadata such as the lengths of line segments, which will be discussed in this work. The G-code parsing, analysis and.vtk export is similar to the procedure described in Englert et al. (2020). The software can be accessed at https://sourceforge.net/projects/ctfam/.

2.2. μCT image acquisition

μCT images were recorded on a YXLON Precision μCT using acceleration voltages between 120 and 200 kV and different target currents. The X-ray tube settings used are provided at the bottom left of each presented image. For each reconstruction 2000 projections over a 360° rotation were recorded on a Perkin Elmer XRD1620 AN flat panel detector with 2048 × 2048 pixels with a pixel pitch of 0.2 mm. Image reconstruction was carried out using VGStudio MAX 3.3 (Volume Graphics GmbH, 2021) using the FDK-algorithm with Shepp-Logan filtering.

2.3. Image analysis

Computed tomography yields a 3D image that can be viewed slice per slice in a discrete viewing plane or it can be studied using various 3D image analysis techniques. One possibility is to run a mathematical function on the grey values at the same position in a stack of slices, e.g. the minimum function, to create a projection image. If h, k, l are indices of a voxel in a volumetric image with the respective grey value $g_{h,k,l}$ and the projection is carried out in the direction of the third index, the grey value $g_{h,k}$ at index h, k in the resulting projection image can be expressed as:

$$g_{h,k} \quad \min_{\forall l \in L} g_{h,k,l}$$

where L is the set of possible indices in the third dimension in the projection range. As defects in tomographic images are displayed by low grey values, taking the minimum of a voxel value of a set of slices and writing the minimum value at each position to a new image yields an image visualising the spatial distribution of pores. This technique is available in many image processing software packages such as ImageJ ("ZProjection") (Schindelin et al., 2012) or VGStudio MAX ("Thick Slab") (Volume Graphics GmbH, 2021). Images produced with this technique will be referred to as projection images in the following.

Each image shown is supplied with an information bar in the bottom which contains from left to right: X-ray tube settings, voxel size, slice or projection image (with depth of projection) with the respective viewing plane orientation (*XY*: perpendicular to the building direction, *XZ/YZ*: parallel to building direction) and a scale bar. Fig. 3 shows the procedure

Table 1
Chemical composition of the AlSi10Mg powder used.

Al	Fe	Si	Mg	Mn	Ti	Zn	Cu	Pb	Sn	Ni
Base	0.14	9.8	0.31	<0.01	0.01	0.01	<0.01	<0.01	<0.01	<0.01

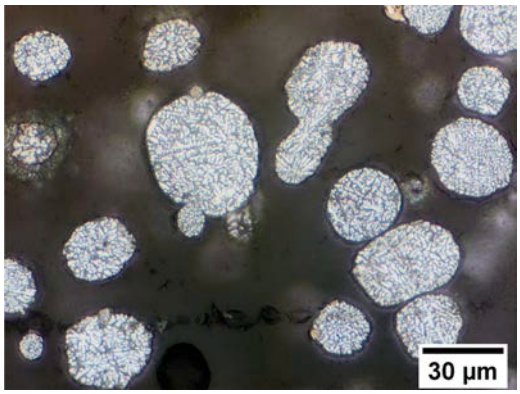

Fig. 1. Cross section of powder used.

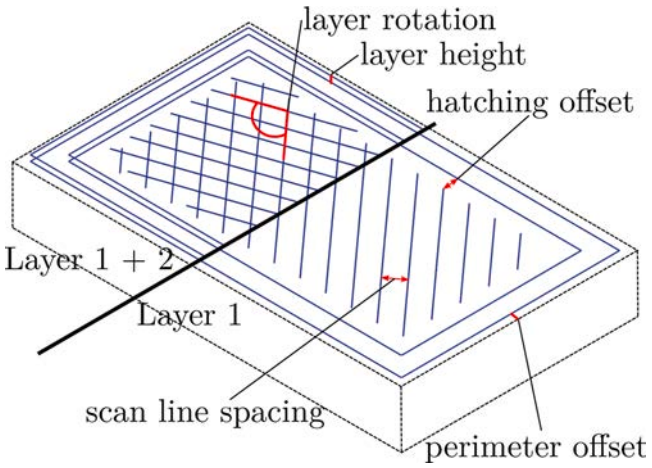

Fig. 2. Sketch of scan pattern used.

on an example image stack, where Fig. 3a shows a slice image compared to Fig. 3c showing a projection image over a depth of 1 mm in building direction, where patterns of high pore count get visible. Porosity values were determined using the VGStudio EasyPore algorithm using a local region of 15 voxels and the relative contrast mode. The contrast value was adjusted for each image for optimal segmentation by visually comparing the result with the input image. Pores smaller than 27 voxels (the volume of a pore with 3 voxels diameter) were filtered out to rule out the influence of noise afflicted grey values being identified as pores. One specimen was analysed for each value. Sphericity analysis was carried out by segmenting volumes in VGStudio EasyPore and analysing the shape of the segmented pores through MorphoLibJ (Legland et al., 2016). MorphoLibJ calculates the sphericity S as the ratio of the squared pore volume V over the cube of the surface area A, i.e.

$$S \quad 36 \times \pi \times V^2/A^3.$$

Spherical pores have a high sphericity, while irregular pores will have low sphericity values ($0 < S \leq 1$).

2.4. Specimen geometries

Different geometries were used to study the influence of parameters and part geometry on defect morphology. The geometries are shown in Fig. 4 and the parameters used for fabricating the geometries are given in Table 2. Geometry A (Fig. 4a) resembles the typical test cube geometry but makes it possible to easily distinguish the different sides of a specimen in the scanned image, by breaking the symmetry with a curved side and a groove. It is used to show the influence of line spacing on defect morphology without major geometrical factors. Geometry B (Fig. 4b) consists of different thin structures, overhangs and grooves. The purpose of this geometry is to test which geometrical factors influence the sensitivity of defect formation on parameters. The thin structures separated by grooves in the centre of the geometry have a thickness of 0.5 mm, while the 45° overhangs in the front are 0.8, 1.2 and 2.2 mm thick. These features will be examined in depth in this work. In Geometry C (Fig. 4c) the tip left in the image (circled red), which has a height of 5 mm and an acute angle of 35°, will be analysed in detail.

Depending on the size of the specimen geometry, different geometrical magnification can be achieved. Geometries A and B were scanned with about 10 µm voxel size, while C was stitched from four single scans to achieve 12.8 µm voxel size. As mentioned, defects smaller than 27 voxels were filtered out to avoid influence of noise, which, when assuming spherical defects, results in a minimum detectable diameter of a pore of about 30 µm for geometries A and B and 40 µm for geometry C.

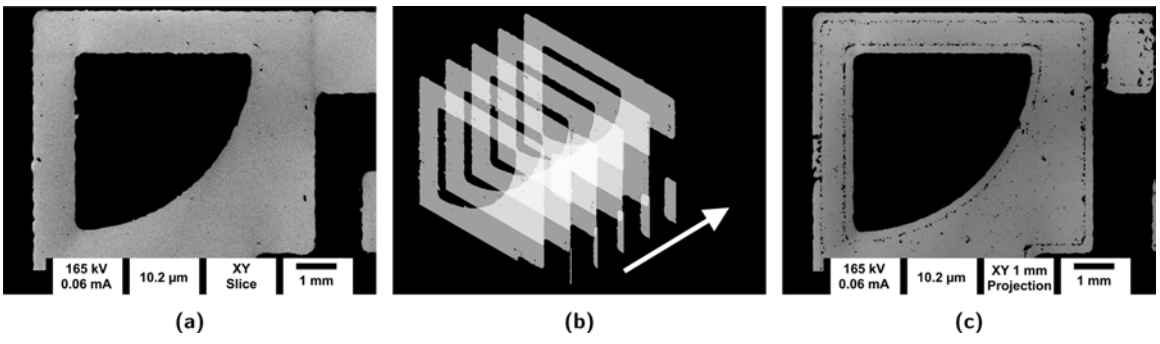

Fig. 3. Example visualisation of projection image generation. (a) Slice image perpendicular to the building direction. (b) 3D visualisation of slice images in building direction. (c) Resulting image from the minimum of slices in a 1 mm thick slab of slices.

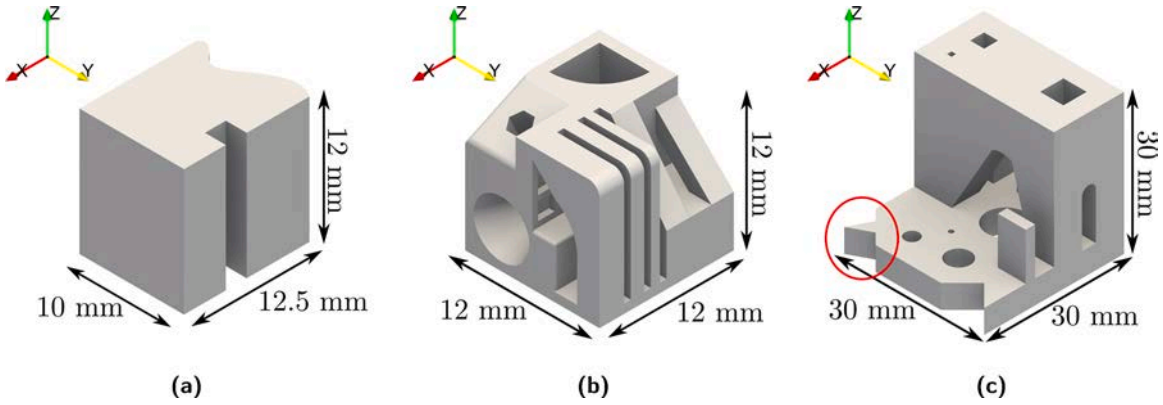

Fig. 4. CAD rendering of investigated geometries. (a) Geometry A, (b) geometry B, (c) geometry C. In geometry C the tip left in the image (circled red) will be analysed in detail. The *Z*-direction is equivalent to the building direction. (For interpretation of the references to colour in this figure citation, the reader is referred to the web version of this article).

Table 2
Parameters used to fabricate the geometries.

Geometry	Laser power in W	Scan speed in mm s ^{1}	Line spacing in µm
A	225	1000	40–220
B	225	600, 1400	100
C	225	1000	190

3. Results

3.1. Effect of line spacing on defect size and morphology

First of all, the variation in the defects visible in µCT images when changing scan line spacing is presented. As a starting point, Geometry A (see Fig. 4a for reference) was manufactured with 225 W laser power and 1000 mm s^{-1} scan speed and varying line distances in 30 µm steps

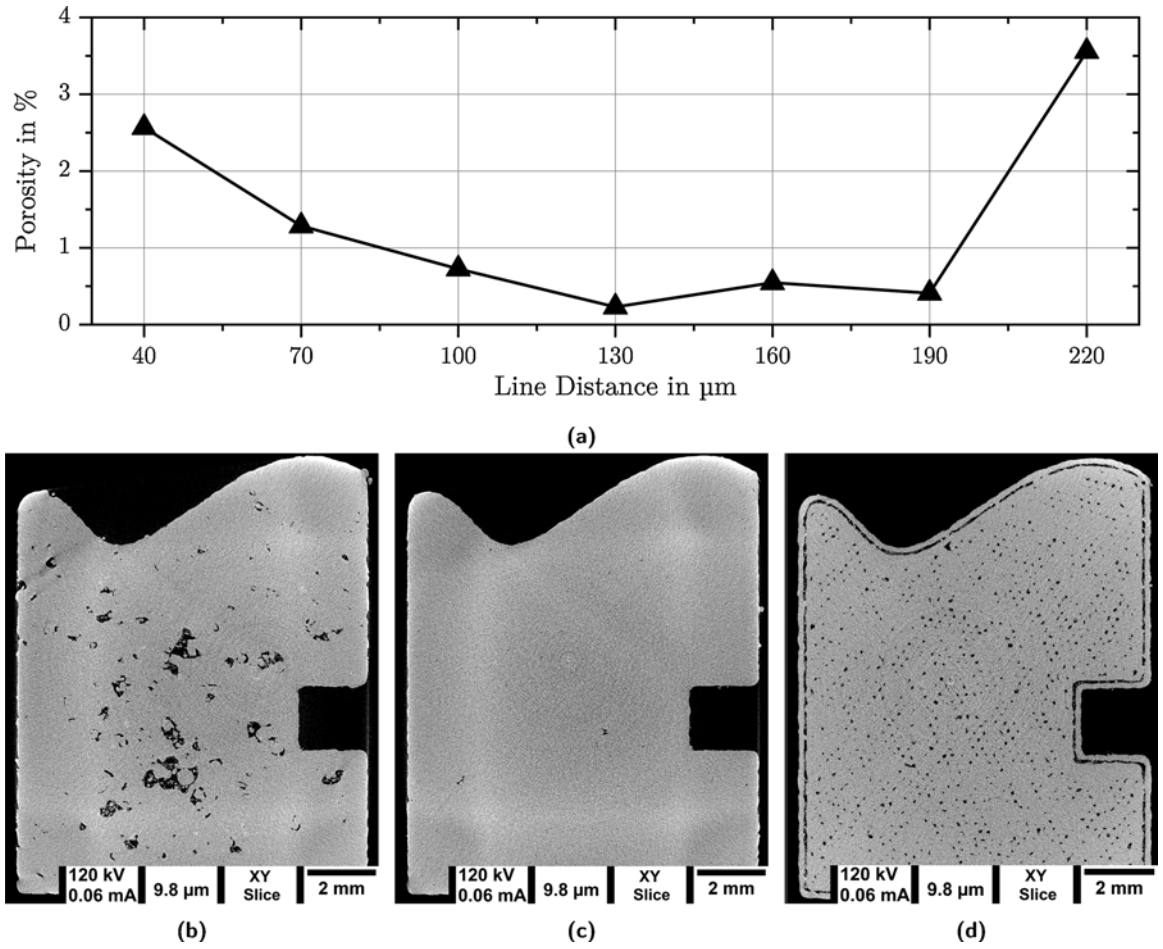

Fig. 5. (a) shows the porosity in specimens with variation of scan line distance. Too large as well as too small line spacing leads to increased porosity. Comparison of defects at (b) small (40 µm), (c) medium (130 µm) and (d) large (220 µm) scan line spacing in geometry A. The specimens were manufactured with 225 W laser power and 1000 mm s ^{1} scan speed, resulting in levels of 2.58% (b), 0.08% (c) and 4.21% (d) porosity measured through µCT.

from 40 to 220 µm. The results of density measurement following Archimedes' principle for each specimen are shown in Fig. 5(a). Line distances between 100 and 190µm produced reasonable porosity values, especially a line distance of 130 µm resulted in the lowest porosity of 0.23% at a reference density of 2.67 g cm^{-3}. Higher as well as lower line distances resulted in higher porosity values. Subsequently a specimen with low line distance (40 µm), high line distance (220 µm) and the optimum value of 130 µm were examined in µCT. Measurement of porosity in the specimen with 130 µm line distance through µCT yielded 0.08% porosity. As discussed in literature (see the works of Damon et al. (2018) or Spierings et al. (2011) for a detailed comparison of both density measurement methods) this is in the range of common deviations between the measurement methods. Especially the uncertainty in the reference density of the LPBF material for the Archimedes method and the neglecting of small defects in µCT measurements due to the resolution limit are reasons for this deviations. Fig. 5c shows a slice image perpendicular to the build direction (*Z*-direction) of a sample manufactured at this setting with only minor small defects, showing the general adequacy of scan speed and laser power settings. Larger line spacing results in a higher porosity value while smaller line spacing also increases porosity. To assess the evolution of the type of pores over the variation of hatch width, the samples were measured through µCT. In the following, a characteristic example of porosity caused by too high line spacing and porosity caused by too low line spacing is examined.

Fig. 5d shows a slice image of a sample manufactured with 220 µm scan line spacing, which contains large regularly spaced pores (4.21% porosity). The pores are nearly triangular exhibiting approximately 67° angles resulting from the shift in layer rotation. As the distance between the two perimeter lines was also increased, the boundary of the specimen is nearly separated from its inner region. In contrast Fig. 5b shows a slice image of a sample produced with 40 µm line spacing exhibiting large irregular pores (2.58% porosity). The pores do not show a regular or periodic pattern like in the 220 µm scan line spacing sample. Some of the pores contain "enclosed" material with a spherical shape.

The distribution of spherical pores, which are mainly attributed to keyhole instability and entrapped gas either from process gas or moisture (see Section 1 for references to literature), can also be observed through µCT images. Fig. 6b shows a slice image through the region where hatching tracks start or end (the slicing plane is illustrated as red line in Fig. 6a) in the sample with 160 µm scan line spacing. Although the specimen only exhibits negligible global porosity (0.1% measured through µCT), it contains a high amount of spherical pores in this region. Fig. 6c shows how porosity is distributed along the Y-direction in the specimen (i.e. from left to right in Fig. 6a). The plotted data for Fig. 6c is produced through VGStudio EasyPore using a step width of five voxels, meaning the porosity in five voxel thick slabs (51 µm) is plotted against their respective position, starting from the lowest to the highest *Y*-index. Fig. 6c shows that porosity in this area is higher than 0.8% compared to a global value of 0.1% porosity. A smaller peak at around 8 mm is caused by pore accumulation near the surface of the groove. Nonetheless, spherical pores also appear statistically distributed in all investigated samples as indicated by the nearly constant background porosity just below 0.1%. The average sphericity of the pores is around 0.84.

3.2. *Effect of overhangs on defects*

To explore possible influences of specimen geometry on the resulting defect distribution, specimen geometries B and C (see Fig. 4b and c for reference) were manufactured using a variation of different process parameters. The geometry B samples (see Fig. 4b) in the following were manufactured with 225 W laser power, 100 µm line spacing and two different scan speed settings of 600 and 1400 mm s^{-1} to evaluate the effect of overhangs on the resulting defects. The global porosity was low in both samples (0.22% in the 600 mm s^{-1} sample and 0.13% in the 1400 mm s^{-1} sample). Nonetheless, locally there exist high defect concentrations at characteristic positions in each specimen. In the following, the three struts with varying thickness in geometry B (see Fig. 4b for reference) with an overhanging surface manufactured with 45° angle and no internal support structures are examined in detail. The struts have a nominal thickness of 0.8, 1.2 and 2.2 mm respectively. Fig. 7 shows minimum projection images with a depth of 0.5 mm of the overhangs manufactured at the two different scan speeds. The projection images make sure that a representative volume of the struts is displayed and accumulations of defects become visible.

At the low scan speed setting (600 mm s^{-1}), the material has a high spherical pore count at the overhanging boundary zone. This can be observed for all widths but the porosity is higher, the thinner the overhang. At the higher scan speed setting (1400 mm s^{-1}) this accumulation occurs only at the thinnest overhang and is less pronounced. On the other hand, large non-spherical pores occur near the vertical surface on the opposite side at the interface between perimeter and hatching. The large quantity of irregular pores visible in the 0.8 mm thick strut, stems from the same kind of perimeter-hatching interface defect in the *Y–Z* plane. These pores are visible because part of this interface region is contained in the projected volume for the thinnest strut.

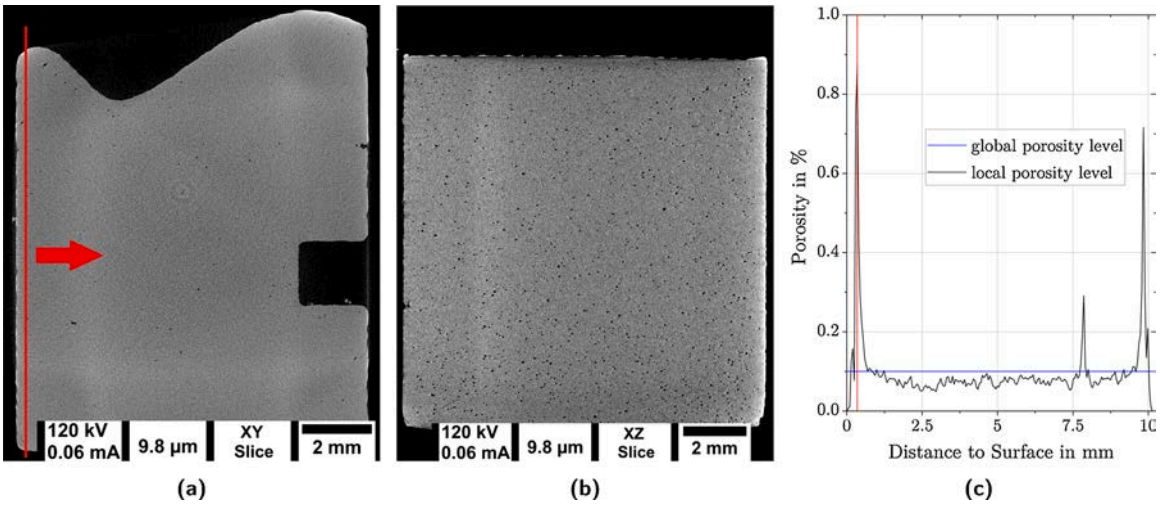

Fig. 6. Slice images of *XY* (a) and *XZ* (b) plane of geometry A. The red line in (a) illustrates the viewing plane of (b). (c) shows the distribution of porosity from the left side to the right side as displayed in (a). The specimen was manufactured with 160 µm line spacing, 225 W laser power and 1000 mm s^{-1} scan speed (0.1% porosity). (For interpretation of the references to colour in this figure legend, the reader is referred to the web version of this article).

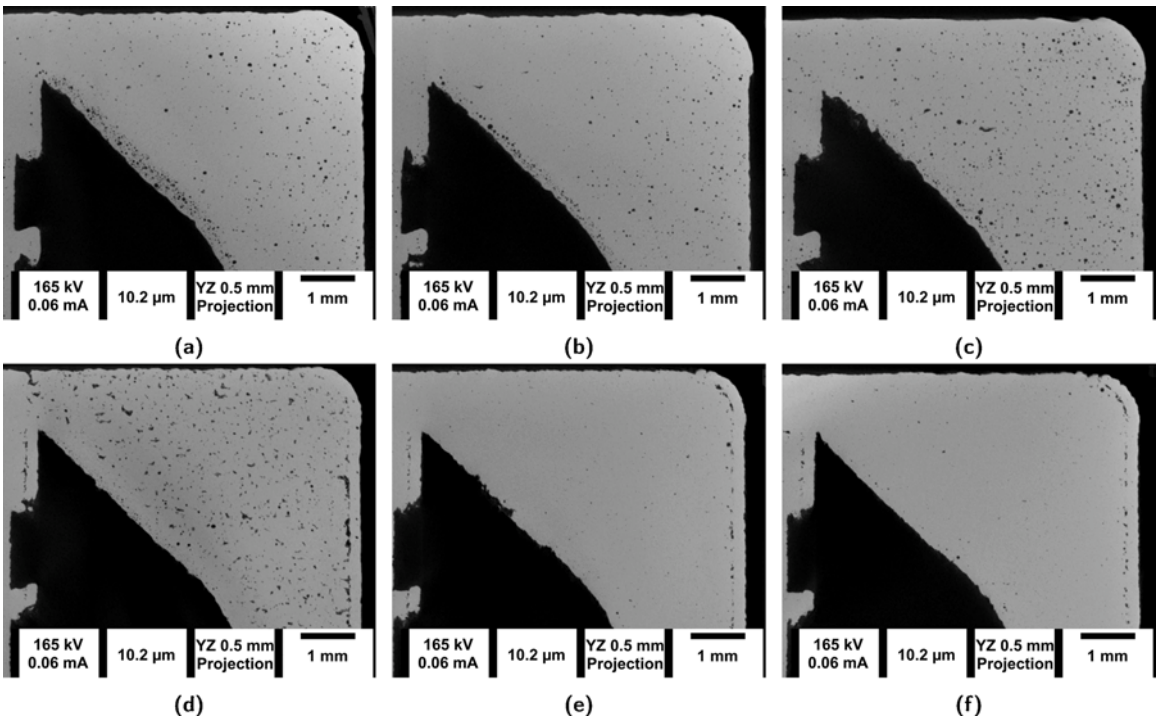

Fig. 7. Projection images (depth = 0.5 mm) showing occurrence of spherical pores at overhangs in geometry B of varying width at two different scan speed settings of 600 and 1400 mm s ^{1} resulting in a porosity of 0.22% for the sample with 600 mm s ^{1} scan speed respectively 0.13% porosity for the sample with 1400 mm s ^{1} scan speed. (a)–(c) 600 mm s ^{1} scan speed, (c)–(e) 1400 mm s ^{1} scan speed. (a) and (c) 0.8 mm strut width, (b) and (d) 1.2 mm strut width, (e) and (f) 2.2 mm strut width.

Fig. 8 shows the distribution of porosity as a function of distance to the overhanging surface of the investigated structures (see Fig. 8a). This graph is produced by analysing porosity along the direction normal to this surface through VGStudio EasyPore using a step width of five voxels, meaning the porosity in five voxel thick slabs (51 µm) is plotted against their respective position. It can be seen that although the global porosity is well below 1%, the overhang causes a significant increase of porosity near the surface when the scan speed is low, especially in thin structures. In contrast, this occurrence of high amounts of spherical porosity near the overhanging surface doesn't happen at high scan speed. The peak in porosity in the fast scanned sample is caused by lack of fusion between hatching and perimeter at the vertical surface of the opposite side, which leads to a high local porosity.

3.3. *Effect of structure size on defects*

Furthermore, geometric features with small wall thicknesses were analysed for defects. In geometry B especially the "groove" type geometry, visible in Fig. 9a, was examined. The undercut groove features are 1.5 mm wide and the separating structures between are 500 µm thick. The specimens shown in Fig. 9 were sliced using a line spacing of 100 µm with two perimeter lines. For the thin features this means: The slicing software applies an offset to the outer perimeter line to account for the width of the outer weld bead to match the geometric specifications of the.stl file. The offset used in this case was 30 µm, which, with the line spacing of 100 µm and the offset between hatching and perimeter (80 µm in this instance), leads to an outer width of 440 µm and an inner width that should be filled with hatching of 80 µm (see Fig. 2 for a graphic explanation of the terms).

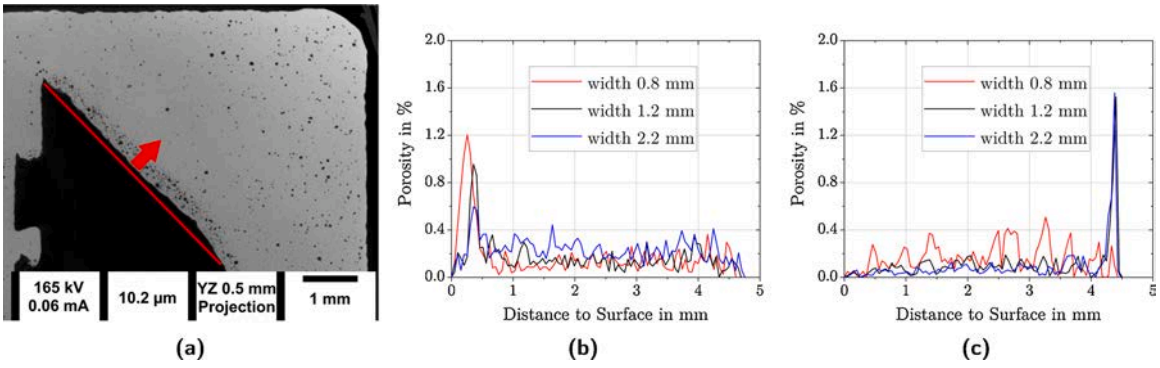

Fig. 8. Distribution of porosity over distance to overhanging surface in the two different scan speed samples overhanging region of geometry B. (a) visualises the direction for porosity analysis in (b) and (c) on the example of the 0.8 mm wide overhang in the 600 mm s ^{1} scan speed sample. (b) shows the porosity distribution in the struts in the 600 mm s ^{1} scan speed sample, while (c) shows the porosity distribution in the struts in the 1400 mm s ^{1} scan speed sample. The occurrence of spherical porosity at overhangs is amplified by thin structures. Another peak in porosity can be observed near the upper surface in the high scan speed sample due to lack of fusion between infill and perimeter.

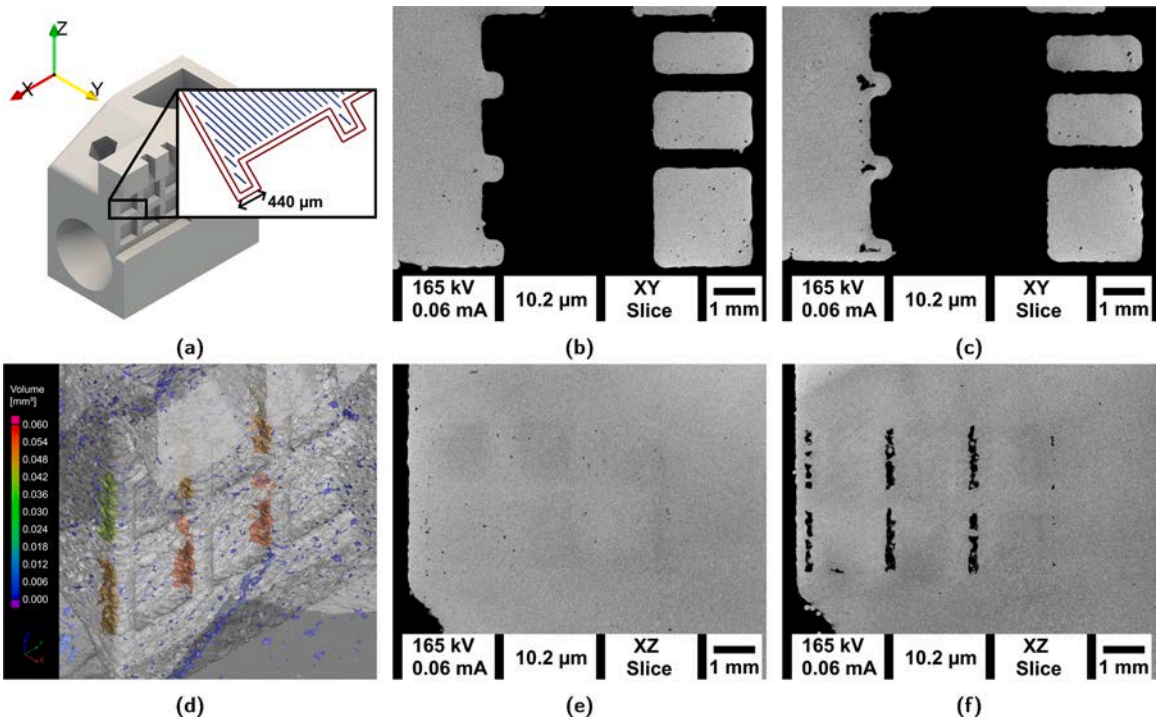

Fig. 9. Defect microstructure in different samples of geometry B. (a) shows the CAD drawing of the inspected geometry with the laser path at the examined area. (d) shows a 3D rendering of the examined location in the high scan speed sample. (b) and (e) show slice images of the sample printed with 600 mm s ^{1} while (c) and (f) show slice images of the sample printed with 1400 mm s ^{1}.

Fig. 9b, c, e and f shows slice images of the mentioned area in geometry B. In Fig. 9c a large irregular pore is visible in each of the 0.5 mm wide structures, whereas the slice image of the sample with 600 mm s^{-1} shows no such defects. Fig. 9e and f show slice images of the specimens parallel to build direction. In the fast scanned sample, the pore is existent in every layer over the building direction, whereas the sample with low scan speed displays no such defect, although it is manufactured with the same scan line spacing. Global porosity in these samples is relatively low (0.22% in the low scan speed sample and 0.13% in the high scan speed sample) emphasising the importance of local defect evaluation.

Another thin structure that was examined is the prismatic tip from the lower section of geometry C. Fig. 10a shows the slice plane used in Fig. 10b (green). The slice image shows a large defect parallel to the vertical surface in the tip. The upper pore is approximately 2 mm long, about 200 µm below it is a cluster of several large pores which is about 1.4 mm in length. This pores are separated by a few material links that are around 100 µm wide. A 500 µm long elongated pore is situated near the bottom of the region. The specimen was manufactured with 225 W laser power, 1000 mm s^{-1} scan speed and 190 µm scan line spacing, which results in a low level of statistically distributed porosity in the inner region of the tip. However the large defect spans through most of the layers and is only connected to some small material links to the perimeter region.

4. Discussion

4.1. Process window characterisation through defect evaluation

The µCT images and measurement data presented allow an assessment of the prevailing mechanism responsible for pore formation in each case.

Lack of fusion. Depending on the employed process parameters, the shape of a molten and solidified track varies. The width of a single melt bead depends on the laser power, scan speed and beam diameter. If the distance between melt beads is just slightly above the bead width, resulting lack of fusion can be at least partially closed by subsequent layers that are rotated with respect to the last layers scan direction, because the weld depth exceeds layer height. At too high line spacing,

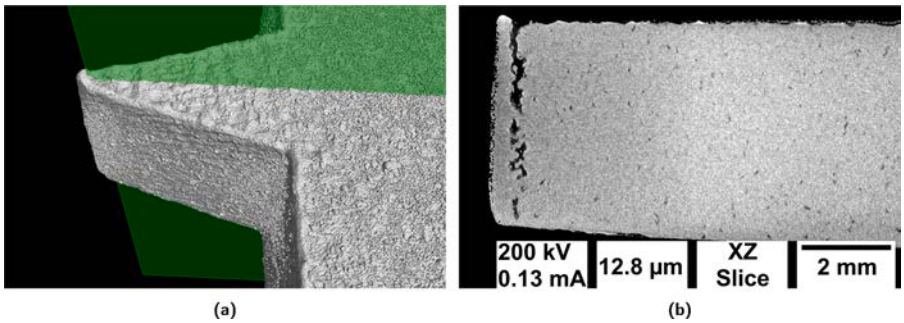

Fig. 10. Defect in a specimen of geometry C manufactured with 225 W laser power, 1000 mm s ^{1} scan speed and 190 µm scan spacing, 0.68% porosity. (a) shows a 3D visualisation of the examined structure of geometry C. (b) shows a slice image parallel to building direction revealing the extent of the defect. (For interpretation of the references to colour in this figure citation, the reader is referred to the web version of this article).

characteristic lack of fusion pores, that show a shape depending on the rotation angle, occur. Fig. 5c shows a slice image of a sample manufactured with line spacing slightly below the measured single bead width of about 150 µm, resulting in a low defect volume and size. In contrast, the line spacing of 220 µm of the sample in Fig. 11b was well above that limit and shows nearly triangular pores exhibiting approximately 67° angles resulting from the layer rotation. Because laser power and scan speed do influence the bead width, higher scan speed and lower laser power lead to lack of fusion even in smaller scan line spacing. This effect is primarily responsible for the effect shown in Fig. 9 or the large pores between hatching and perimeter visible in the 1400 mm s^{-1} scan speed samples but not in the 600 mm s^{-1} scan speed samples (cf. Fig. 7c–f). Gan et al. (2021) investigated a scaling law for the LPBF process accounting for various effects including thermal conductivity. Such laws could be further improved by taking into account the different heat dissipation of the built geometries to reflect effects like the observed phenomenon. This would allow for finding this phenomenon with other parameter combinations as well.

Instabilities. At inappropriate process settings an instability of the weld beads occurs where surface tension of the molten metal leads to a form of the Plateau-Rayleigh instability that forms droplets out of the weld beads. Especially low scan line spacing leads to this behaviour. The surface of the last molten layer is distorted by this behaviour and impairs uniform spreading of the subsequent powder layer. Similar behaviour is reported for too low power or too high scan speed as balling in literature (e.g. Aboulkhair et al., 2014). This effect can be ruled out here, as these settings were left constant for geometry A. Fig. 11a shows a detail view of a typical defect of a sample manufactured at a low scan spacing of 40 µm, showing large irregular pores that are not related to the kind of lack of fusion defect visible in Fig. 11b, since no systematic orientation is visible. In contrast, some of the pores seem to enclose spherical portions of material. A measurement of the spherical material at two locations yields a diameter of >400 µm, which is larger than the D90 of the powder used and larger than the material between lack of fusion pores in the specimen manufactured with 220 µm line spacing. The presumption is that these defects stem from either the weld beads becoming droplets, therefore distorting even material deposition or leading to insufficient powder spreading near these defects. An explanatory sketch of the presumed mechanism is shown in Fig. 12. The first laser irradiation spot (shown in red (t_0)) is moving out of the sketch plane. Depending on the line spacing, powder or solidified metal gets irradiated by the subsequent scan vector (t_1). The laser light is absorbed by a higher proportion of already solidified metal with a high thermal conduction coefficient instead of hitting the more isolating powder bed, where the heat is dissipated more slowly (see Wang et al. (2019) for calculations on conductivity of the powder bed). In addition, studies have shown higher absorptivity in the powder bed compared to solidified metal due to multiple reflections of the laser light between particles (see Yang et al., 2018b and Gusarov and Kruth, 2005). These mechanisms result in less energy available to melt the powder, which in turn results in an altered bead geometry that seems to be highly susceptible to the Plateau-Rayleigh instability.

Keyhole porosity. This investigation showed keyhole pore concentration present at the interface between hatching and perimeter (see Fig. 6b for reference). The underlying mechanisms of how these defects arise have already been discussed in literature (see Martin et al., 2019 or Yang et al., 2018a). The presented results help in understanding the extent of this kind of defect formation mechanism. In the shown sample, keyhole pore formation is the predominant mechanism. However, the relative porosity remains low even if measured locally in the interface area prone to keyhole porosity. The mean sphericity of all pores in the perimeter-hatching interface region (i.e. at the first peak in Fig. 6c) is over 0.9, which is known to result in a lower criticality for crack initiation of the defect shape in contrast to, e.g. lack-of-fusion pores (see Nadot et al., 2020). Nonetheless, their position near the surface makes these defects critical for fatigue performance as shown by Yang et al. (2018a).

4.2. Local process – microstructure relationships

Struts manufactured with high scan speed show lack of fusion porosity at all non-overhanging boundary zones (cf. Fig. 7c, d and f). This could be eliminated by reducing the spacing between hatching and perimeter for this scan speed setting. More interestingly, there is no lack of fusion between the inner area and the overhanging surface, which means the melt pool is wider in this location, so the spacing is not too wide there. Low scan speed leads to the formation of a high count of small spherical pores near the overhanging surface. It can be seen that especially thinner struts are more susceptible to the formation of these pores and wider struts show reduced spherical porosity even at low scan speed. It can be reasoned that the wider structures allow for a fast enough heat transfer away from the process zone, reducing overheating in the melt pool. High scan speed reduces energy that is transferred into the melt pool in the first place, also reducing risk of overheating. In the thinnest fast scanned overhang there is also a small accumulation of spherical pores, so it seems the energy input is still too high for this geometry (see Fig. 7c). The porosity distribution plot in Fig. 8c does not show this accumulation of pores visible in the projection image, which is due to the minimum size of 27 voxels for each individual pore that is captured by our method. The pores are too small to be safely identified by µCT. Because of this, also the values of porosity near the overhanging surface for the 600 mm s^{-1} scan speed sample shown in Fig. 8b are likely underestimated. These structures should be ground and polished in subsequent work to evaluate porosity, but the qualitative aspect of the images shown is enough for the argumentation of this work.

The lack of fusion porosity shown in Fig. 5d can easily be avoided by tuning the scan line spacing parameter to smaller values until low porosity values are achieved. Then again, lower bounds on the line spacing should be considered and introduced to avoid melt pool instability leading to irregular porosity as shown in Fig. 5b. More threatening, however, is the kind of defect formation shown in the small structures of sample B (shown in Fig. 9) and the prismatic tip structure of

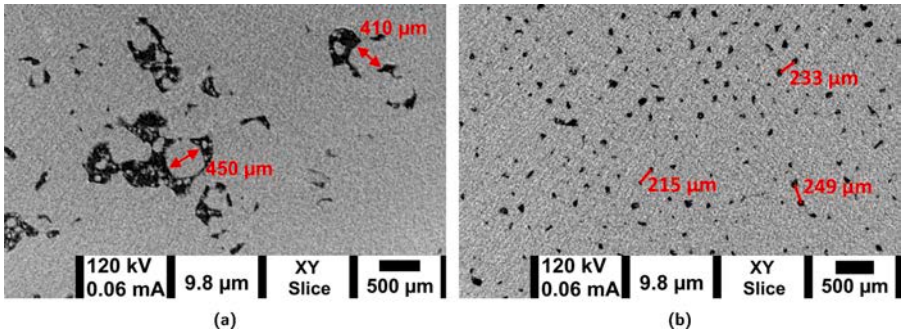

Fig. 11. Detailed views of defects in specimens of geometry A depending on line spacing. (a) 40 µm scan line spacing. (b) 220 µm scan line spacing.

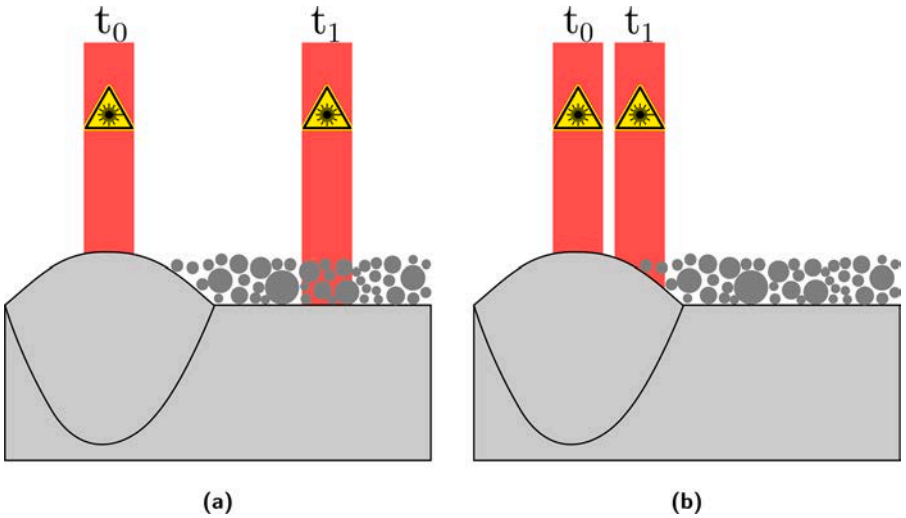

Fig. 12. Process sketch in a medium line spacing (a) and small line spacing (b) situation. The first scan line is denoted by t_0 and the second scan line by t_1. Depending on line spacing, the laser spot hits solidified metal or the powder bed. (For interpretation of the references to colour in this figure citation, the reader is referred to the web version of this article).

sample C (shown in Fig. 10). This kind of lack of fusion pore is not directly caused by inappropriate process settings, but by scan strategy, machine or software limitations. In the following, we point to the manufactured paths of the regions of samples B and C shown in Fig. 13. As explained above, the part of the thin wall in geometry B that has to be hatched is 240 µm wide. When also subtracting the offset of 80 µm distance between hatching and perimeter, the width is reduced to 80 µm. Depending on the rotation angle in each layer, different line lengths have to be scanned. Analysis of the manufactured path through GCode2vtk showed that hatching paths were only placed in very few layers in this location. The shortest path placed in the sample manufactured with 600 mm s^{-1} scan speed was about 150 µm long, while the shortest path placed in the sample manufactured with 1400 mm s^{-1} scan speed was about 350µm long. This length refers to the total length of a path, i.e. the distance travelled between a laser on and a laser off command. The reason for this difference is a minimum laser working time enforced by the slicer software. The value for this time t_{min} provided by the manufacturer is 250 µs. If a line to be scanned is too small, the machine controller would have to turn the laser on and off within a single control cycle which would lead to an error. Thus, the slicer software calculates the smallest possible line length L_{min} for the scan speed v_{scan} used through $L_{min} \quad v_{scan} * t_{min}$ and filters out lines smaller than this value.

Fig. 13a shows a comparison of the laser trajectories of the 600 mm s^{-1} scan speed and 1400 mm s^{-1} scan speed samples in the thin structure between the grooves. This location corresponds to the location with the large defect presented in Fig. 9. It is evident that the fast scanned sample is scanned sparsely, but also the path density in the slow scanned sample is reduced compared to the inner region of the sample. However no lack of fusion defects can be found in Fig. 9e, so the cause of defect formation is twofold: Higher scan speed induces sparser path placement and at the same time smaller bead widths (see Aboulkhair et al. (2016) or Kempen et al. (2011) for investigations on the influence of scan speed on bead width). Higher bead widths induced by slow scan speed, hinder the formation of lack of fusion pores even at higher scan line spacing. Fig. 13b shows the laser trajectory of two layers in the tip

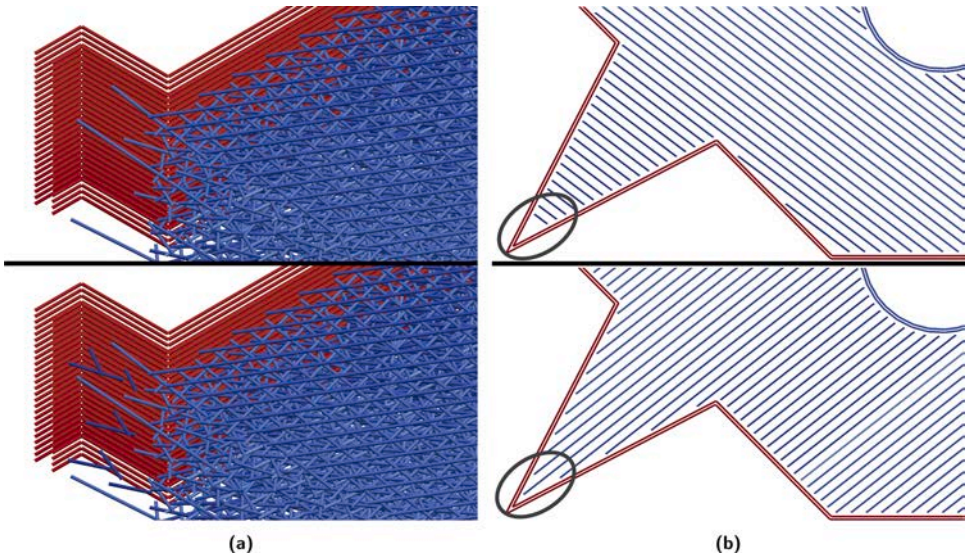

Fig. 13. Trajectories in thin features of geometries B and C (red: perimeter, blue: hatching). (a) Comparison of trajectory in thin structures of geometry B at 600 mm s^{-1} (bottom) and 1400 mm s^{-1} (top) scan speed. (b) Trajectory in geometry C in a layer with high coverage (bottom) and low coverage (top) of the tip structure. (For interpretation of the references to colour in this figure legend, the reader is referred to the web version of this article).

structure presented in Fig. 10b as another example of the revealed mechanism. Similar to the mechanisms involved in the thin structures of geometry B, the inner structure of the tip is not filled properly. Depending on the rotation angle in the respective layer, some of the paths get filtered out which leads to too sparse filling of the area and ultimately to a large lack of fusion pore under the surface of the specimen. The minimal line length for this sample was about 250 μm.

5. Conclusion

The results presented show how component geometry and process parameters interact in the formation of defects in additively manufactured components.

- When manufacturing complicated geometries, the slicing algorithm starts to play an important role in examining defect formation. Trajectories in thin geometries are prone to violate line length criteria of the slicer and thus the effective scan line spacing in these areas is increased.
- The process parameters, often only described in optimising global density, can be used to control geometry induced defect formation. Low scan speed allows filling of areas where line spacing is higher, whereas high scan speed, due to reduced bead width, creates large irregular pores. This relationship also allows to improve the accuracy of manufactured structures.
- Another geometrical implication in component quality is temperature at overhangs. Especially in thin struts, low scan speed leads to the formation of spherical pores near the overhanging surface. This effect led to more than a fivefold increase in porosity near the overhanging surface compared to the global porosity value. High scan speed mitigates this problem at least partially.

When considering all of the effects mentioned, it becomes clear that parameters will need to be adjusted locally to account for these effects and to obtain components with a minimum of defects. To this end, optimised parameters for various geometric elements have to be found. This could be done on the basis of empirical experiments or simulations. Another possibility is to allow trajectory planning software to adjust line spacing in a permissible range to avoid formation of lack of fusion pores.

Future work should concentrate on a higher variability of laser processing parameters and a detailed correlation to basic engineering geometries. Such investigations have the potential to yield an adaptive selection strategy of process settings like scan line spacing and scan speed depending on local geometry. In addition, effects from the build plate position or temperature build up should be measured and could be included in the scan strategy.

Authors' contribution

Lukas Englert: data curation, writing – original draft, software. Steffen Czink: methodology, investigation. Stefan Dietrich: conceptualisation, writing – review & editing. Volker Schulze: supervision, writing – review & editing.

Conflict of interest

None declared.

Declaration of Competing Interest

The authors report no declarations of interest.

Acknowledgements

Funding by the German Research Foundation (DFG) within the Project "Material- and process oriented non-destructive testing of additively manufactured components by computed tomography" (Project number 398368987) for this research is gratefully acknowledged.

References

Aboulkhair, N.T., Everitt, N.M., Ashcroft, I., Tuck, C., 2014. Reducing porosity in AlSi10Mg parts processed by selective laser melting. Addit. Manuf. 1–4, 77–86. https://doi.org/10.1016/j.addma.2014.08.001.

Aboulkhair, N.T., Maskery, I., Tuck, C., Ashcroft, I., Everitt, N.M., 2016. On the formation of AlSi10Mg single tracks and layers in selective laser melting: microstructure and nano-mechanical properties. J. Mater. Process. Technol. 230, 88–98. https://doi.org/10.1016/j.jmatprotec.2015.11.016.

Ahrens, J., Geveci, B., Law, C., 2005. Paraview: an end-user tool for large data visualization. The Visualization Handbook 717.

Cunningham, R., Zhao, C., Parab, N., Kantzos, C., Pauza, J., Fezzaa, K., Sun, T., Rollett, A. D., 2019. Keyhole threshold and morphology in laser melting revealed by ultrahigh-speed X-ray imaging. Science 363, 849–852. https://doi.org/10.1126/science.aav4687.

Damon, J., Dietrich, S., Vollert, F., Gibmeier, J., Schulze, V., 2018. Process dependent porosity and the influence of shot peening on porosity morphology regarding selective laser melted AlSi10Mg parts. Addit. Manuf. 20, 77–89. https://doi.org/10.1016/j.addma.2018.01.001.

DebRoy, T., Wei, H.L., Zuback, J.S., Mukherjee, T., Elmer, J.W., Milewski, J.O., Beese, A. M., Wilson-Heid, A., De, A., Zhang, W., 2018. Additive manufacturing of metallic components – process, structure and properties. Prog. Mater. Sci. 92, 112–224. https://doi.org/10.1016/j.pmatsci.2017.10.001.

Dong, Z., Zhang, X., Shi, W., Zhou, H., Lei, H., Liang, J., 2018. Study of size effect on microstructure and mechanical properties of AlSi10Mg samples made by selective laser melting. Materials 11, 2463. https://doi.org/10.3390/ma11122463.

Du Plessis, A., 2019. Effects of process parameters on porosity in laser powder bed fusion revealed by X-ray tomography. Addit. Manuf. 30, 100871. https://doi.org/10.1016/j.addma.2019.100871.

Englert, L., Dietrich, S., Pinter, P., 2020. Investigations on printing path dependent properties of additively manufactured samples using micro computed tomography. Rapid Prototyp. J. https://doi.org/10.1108/RPJ-07-2019-0200.

Gan, Z., Kafka, O.L., Parab, N., Zhao, C., Fang, L., Heinonen, O., Sun, T., Liu, W.K., 2021. Universal scaling laws of keyhole stability and porosity in 3d printing of metals. Nat. Commun. 12, 1–8. https://doi.org/10.1038/s41467-021-22704-0.

Gusarov, A., Kruth, J.P., 2005. Modelling of radiation transfer in metallic powders at laser treatment. Int. J. Heat Mass Transfer 48, 3423–3434. https://doi.org/10.1016/j.ijheatmasstransfer.2005.01.044.

Hastie, J.C., Kartal, M.E., Carter, L.N., Attallah, M.M., Mulvihill, D.M., 2020. Classifying shape of internal pores within AlSi10Mg alloy manufactured by laser powder bed fusion using 3D X-ray micro computed tomography: influence of processing parameters and heat treatment. Mater. Charact. 110225. https://doi.org/10.1016/j.matchar.2020.110225.

Kempen, K., Thijs, L., Yasa, E., Badrossamay, M., Verheecke, W., Kruth, J., 2011. Process optimization and microstructural analysis for selective laser melting of AlSi10Mg. Solid Freeform Fabrication Symposium 484–495.

Legland, D., Arganda-Carreras, I., Andrey, P., 2016. MorphoLibJ: integrated library and plugins for mathematical morphology with ImageJ. Bioinformatics 32, 3532–3534. https://doi.org/10.1093/bioinformatics/btw413.

Léonard, F., Tammas-Williams, S., Prangnell, P.B., Todd, I., Withers, P.J., 2012. Assessment by X-ray CT of the effects of geometry and build direction on defects in titanium ALM parts. Conference on Industrial Computed Tomography (iCT) 19–21.

Martin, A.A., Calta, N.P., Khairallah, S.A., Wang, J., Depond, P.J., Fong, A.Y., Thampy, V., Guss, G.M., Kiss, A.M., Stone, K.H., et al., 2019. Dynamics of pore formation during laser powder bed fusion additive manufacturing. Nat. Commun. 10, 1–10. https://doi.org/10.1038/s41467-019-10009-2.

Matthews, M.J., Guss, G., Khairallah, S.A., Rubenchik, A.M., Depond, P.J., King, W.E., 2016. Denudation of metal powder layers in laser powder bed fusion processes. Acta Mater. 114, 33–42. https://doi.org/10.1016/j.actamat.2016.05.017.

Nadot, Y., Nadot-Martin, C., Kan, W.H., Boufadene, S., Foley, M., Cairney, J., Proust, G., Ridosz, L., 2020. Predicting the fatigue life of an AlSi10Mg alloy manufactured via laser powder bed fusion by using data from computed tomography. Addit. Manuf. 32, 100899. https://doi.org/10.1016/j.addma.2019.100899.

O.R. Lasertechnologie GmbH, 2021. Orlas Suite (Accessed 29 January 2021). https://www.or-laser.com/de/software/orlas-suite/.

Piazza, S., Merrigan, B., Dowling, D.P., Celikin, M., 2020. The effects of geometry and laser power on the porosity and melt pool formation in additively manufactured 316l stainless steel. Int. J. Adv. Manuf. Technol. 111, 1457–1470. https://doi.org/10.1007/s00170-020-06196-8.

Prashanth, K., Scudino, S., Maity, T., Das, J., Eckert, J., 2017. Is the energy density a reliable parameter for materials synthesis by selective laser melting? Mater. Res. Lett. 5, 386–390. https://doi.org/10.1080/21663831.2017.1299808.

Roach, A.M., White, B.C., Garland, A., Jared, B.H., Carroll, J.D., Boyce, B.L., 2020. Size-dependent stochastic tensile properties in additively manufactured 316L stainless steel. Addit. Manuf. 32, 101090. https://doi.org/10.1016/j.addma.2020.101090.

Sanaei, N., Fatemi, A., Phan, N., 2019. Defect characteristics and analysis of their variability in metal L-PBF additive manufacturing. Mater. Des. 182, 108091. https://doi.org/10.1016/j.matdes.2019.108091.

Schindelin, J., Arganda-Carreras, I., Frise, E., Kaynig, V., Longair, M., Pietzsch, T., Preibisch, S., Rueden, C., Saalfeld, S., Schmid, B., et al., 2012. Fiji: an open-source platform for biological-image analysis. Nat. Methods 9, 676–682. https://doi.org/10.1038/nmeth.2019.

Scipioni Bertoli, U., Wolfer, A.J., Matthews, M.J., Delplanque, J.P.R., Schoenung, J.M., 2017. On the limitations of Volumetric Energy Density as a design parameter for selective laser melting. Mater. Des. 113, 331–340. https://doi.org/10.1016/j.matdes.2016.10.037.

Spierings, A., Schneider, M., Eggenberger, R., 2011. Comparison of density measurement techniques for additive manufactured metallic parts. Rapid Prototyp. J. 17, 380–386. https://doi.org/10.1108/13552541111156504.

Takata, N., Kodaira, H., Suzuki, A., Kobashi, M., 2018. Size dependence of microstructure of AlSi10Mg alloy fabricated by selective laser melting. Mater. Charact. 143, 18–26. https://doi.org/10.1016/j.matchar.2017.11.052.

Volume Graphics GmbH, 2021. Vgstudio Max (Accessed 29 January 2021). https://www.volumegraphics.com/de/produkte/vgstudio-max.html.

Wang, P., Lei, H., Zhu, X., Chen, H., Fang, D., 2019. Influence of AlSi10Mg particles microstructure on heat conduction during additive manufacturing. Int. J. Heat Mass Transfer 144, 118632. https://doi.org/10.1016/j.ijheatmasstransfer.2019.118632.

Yang, K.V., Rometsch, P., Jarvis, T., Rao, J., Cao, S., Davies, C., Wu, X., 2018a. Porosity formation mechanisms and fatigue response in Al-Si-Mg alloys made by selective laser melting. Mater. Sci. Eng. A 712, 166–174. https://doi.org/10.1016/j.msea.2017.11.078.

Yang, Y., Gu, D., Dai, D., Ma, C., 2018b. Laser energy absorption behavior of powder particles using ray tracing method during selective laser melting additive manufacturing of aluminum alloy. Mater. Des. 143, 12–19. https://doi.org/10.1016/j.matdes.2018.01.043.